

Changes in the Interaction between Tropical Convection, Radiation, and the Large-Scale Circulation in a Warming Environment

DEREK J. POSSELT

University of Michigan, Ann Arbor, Ann Arbor, Michigan

SUSAN VAN DEN HEEVER, GRAEME STEPHENS, AND MATTHEW R. IGEL

Colorado State University, Fort Collins, Colorado

(Manuscript received 26 October 2010, in final form 8 July 2011)

ABSTRACT

This paper explores the response of the tropical hydrologic cycle to surface warming through the lens of large-domain cloud-system-resolving model experiments run in a radiative–convective equilibrium framework. Simulations are run for 55 days and are driven with fixed insolation and constant sea surface temperatures (SSTs) of 298 K, 300 K, and 302 K. In each experiment, convection organizes into coherent regions of large-scale ascent separated by areas with relatively clear air and troposphere-deep descent. Aspects of the simulations correspond to observed features of the tropical climate system, including the transition to large precipitation rates above a critical value of total column water vapor, and an increase in convective intensity with SST amidst weakening of the large-scale overturning circulation. However, the authors also find notable changes to the interaction between convection and the environment as the surface warms. In particular, organized convection in simulations with SSTs of 298 and 300 K is inhibited by the presence of a strong midtropospheric stable layer and dry upper troposphere. As a result, there is a decrease in the vigor of deep convection and an increase in stratiform precipitation fraction with an increase in SST from 298 to 300 K. With an increase in SST to 302 K, moistening of the middle troposphere and increase in lower-tropospheric buoyancy serve to overcome these limitations, leading to an overall increase in convective intensity and larger increase in upper-tropospheric relative humidity. The authors conclude that, while convective intensity increases with SST, the aggregate nature of deep convection is strongly affected by the details of the thermodynamic environment in which it develops. In particular, the positive feedback between increasing SST and a moistening upper troposphere found in the simulations, operates as a nonmonotonic function of SST and is modulated by a complex interaction between deep convection and the environmental relative humidity and static stability profile. The results suggest that projected changes in convection that assume a monotonic dependence on SST may constitute an oversimplification.

1. Introduction

Questions of the response of clouds to global warming are central to the current debate over the response of the earth's climate system to increases in greenhouse gas concentrations. Changes in deep convection are of particular interest, as organized deep convection plays a key role in linking the vertical profile of radiative heating and cooling to the large-scale circulation. It is because of this that many of the proposed cloud–radiation feedback mechanisms are predicated on changes to

the characteristics of convection as the planet warms (Stephens 2005). Though studies involving satellite and in situ observations (e.g., Zhang 1993; Sherwood and Wahrlich 1999; Masunaga et al. 2005; Rapp et al. 2005; Su et al. 2006; Rondanelli and Lindzen 2008) have shed light on how deep convection might change in a warming environment, examination of the response of convection to a perturbation in the climate system requires use of a model. Several studies have employed cloud-system-resolving models (CSRMs) to this end, using both horizontally uniform sea surface temperature (SST; e.g., Tompkins and Craig 1998a,b; Bretherton et al. 2005; Kuang and Hartmann 2007; Stephens et al. 2008; Pakula and Stephens 2009) and imposed horizontal SST gradients (Grabowski et al. 2000; Tompkins 2001a,b). Many

Corresponding author address: Derek J. Posselt, University of Michigan, 2455 Hayward St., Ann Arbor, MI 48109-2143.
E-mail: dposselt@umich.edu

modeling studies have employed radiative convective equilibrium (RCE) as a useful framework, exploiting the fact that deep convection produces an adjustment to an equilibrium state that is rapid compared to the time scale of forcing mechanisms. Several decades of research have resulted in a greatly improved understanding of the interaction between deep convection, radiation, and the large-scale overturning (e.g., Hadley and Walker) circulation, yet there remain mysteries associated with the response of the coupled convection–radiation–circulation system to a warming environment. These include 1) how convective organization on the large scale changes with warming, 2) how warming influences the interaction between convection and the environment, including changes to the static stability structure and the relative humidity profile in regions outside of deep convection, and 3) how convective structure changes in a warming environment, including the partition between convective and stratiform precipitation. Complicating matters is the fact that deep convection and the large-scale circulation constitute a mutually interacting system, requiring models that resolve a large range of spatial scales. In addition, correct representation of cloud-system-scale processes requires sophisticated cloud microphysical and radiation schemes capable of realistically simulating the interaction between changes to cloud properties and the radiative budget.

In this paper, we examine the response of organized convection to surface warming using a CSRSM with a state-of-the-art cloud microphysical parameterization scheme run on a domain large enough to capture the large-scale overturning circulation and with a grid spacing small enough to explicitly resolve (albeit rather crudely) deep convective systems and their interaction with the environment. We examine how surface warming affects the interaction between organized convection and the large-scale circulation, then explore the physical mechanisms that underlie a number of intriguing features of the tropical system, including changes in convective intensity with SST, moistening of the upper troposphere, and the observed shift in the character of deep convection as SSTs warm past 300 K. Consistent with previous studies, we find that the large-scale circulation weakens with SST but convective updrafts and precipitation rates intensify. However, as the SST warms from 298 to 302 K, we also find a nonmonotonic change in the fraction of convective precipitation and a shift in both the large-scale organization of convection and in its interaction with the immediate and far-field environment that suggests the presence of a deep convection rate limiter present at SSTs lower than approximately 300 K. As a result, though lower-tropospheric relative humidity remains nearly invariant with warming, the middle and upper troposphere relative humidity increases rather significantly.

The remainder of this paper is structured as follows. In section 2, we describe the model and experimental set up, and provide an overview of the characteristics of the large-scale energy balance and hydrologic cycle at RCE in section 3. We explore the changes to the large-scale circulation and characteristics of convection that arise as SST increases in section 4, and discuss the mechanisms driving the changes observed in simulated convection and the environment in section 5. A summary of our conclusions is offered in section 6.

2. Model description and experimental setup

The cloud system resolving model used in this study is the Regional Atmospheric Modeling System (RAMS), developed at Colorado State University (Pielke et al. 1992; Cotton et al. 2003). The RAMS model includes a detailed bulk cloud microphysical scheme that assumes a gamma-shaped particle size distribution for three species of liquid (small and large cloud droplets and rain) and five species of ice (small and large vapor grown crystals, aggregates, graupel, and hail). Ice crystal habit is allowed to vary as a function of temperature. Consistent with observations of a bimodal cloud droplet size distribution, the cloud droplet spectrum is decomposed into two modes, one for droplets 1–40 μm in diameter, and the second for droplets 40–80 μm in diameter. The RAMS radiation scheme (Harrington et al. 1999) fully interacts with all eight cloud species and accounts for changes in cloud particle size distributions as cloud systems develop and evolve. A Rayleigh friction layer is implemented in the top four model levels to absorb vertically propagating gravity waves, and surface processes are parameterized using the Land Ecosystem–Atmosphere Feedback-2 (LEAF-2) (Walko et al. 2000) scheme. The model's advection scheme, turbulence, radiation, cloud microphysics, and surface flux parameterizations are more fully documented in Cotton et al. (2003), and a detailed description of recent changes to the cloud microphysics can be found in Saleeby and Cotton (2004).

To accommodate development of realistic large-scale overturning circulations, we employ a three-dimensional model domain with doubly periodic boundaries. To address concerns about the use of 3D domains restricted to just a few 100 km in scale we adopt the channel-mode configuration originally introduced by Tompkins (2001a) and employed by Stephens et al. (2008) and Posselt et al. (2008). This configuration represents a compromise between the need for a 3D domain large enough so as not to trivially constrain the behavior of the convective ensemble, yet small enough to meet the limitations of available computer resources. Use of a three-dimensional

canyon-type grid also allows for realistic divergent motions in organized convection, which have been shown to be artificially strong in two-dimensional slab-symmetric experiments at radiative convective equilibrium (Tompkins 2000). Horizontal grid spacing of 2.4 km is used in both zonal and meridional directions, and the vertical grid consists of 38 levels, which stretch gradually from a depth of 20 m in the boundary layer to just over 1 km in the upper troposphere. It should be noted that a 2.4-km horizontal grid spacing, while typical of other CRM-based RCE experiments of this type, only marginally resolves individual deep convective cores, if at all (e.g., Bryan et al. 2003), and shallow and congestus-type convection is not explicitly represented. This resolution does, however, resolve the important interaction between convection and the environment on the mesobeta scale (Moncrieff 2004), which is the primary focus of this study. The 2.4-km grid spacing is also fine enough to obviate the need for a convective parameterization scheme.

All experiments are initialized from the 0000 UTC 5 December 1992 Tropical Ocean and Global Atmosphere Coupled Ocean–Atmosphere Response Experiment (TOGA COARE) sounding with initial zero mean wind in the vertical and fixed and uniform SSTs of 298, 300, and 302 K. Convection is initiated by adding small (less than 0.1 K) random perturbations to the potential temperature field in the lowest 2 km across the entire domain at the initial time, and each simulation is integrated to 55 days. As in past studies of this type, we employ a fixed solar zenith angle of 50° such that the daily insolation is maintained at 447.2 W m^{-2} ; roughly equivalent to the mean annual insolation at the equator. Note that there is no representation of the diurnal cycle in this model configuration and the Coriolis parameter is set equal to zero. While SSTs remain fixed in the respective model runs, the wind field is allowed to evolve as part of the localized turbulence and broader-scale circulations that are established over time.

Equilibrium is attained when the total surface (sensible plus latent) heat fluxes are in balance with the net radiative flux divergence and, from Fig. 1, it can be seen that this is the case as of approximately 40–45 days into each simulation (earlier for the higher-SST runs). Though our simulations attain a state of RCE, it should be noted that it is possible that multiple equilibrium solutions may exist for a given fixed SST (e.g., Sobel et al. 2007; Bellon and Sobel 2010). Computational limitations prevented us from running ensembles of simulations with differing initial conditions and from running simulations with SST between 298 and 300 K and between 300 and 302 K. It should also be mentioned that, while it is common practice to use different but fixed values of

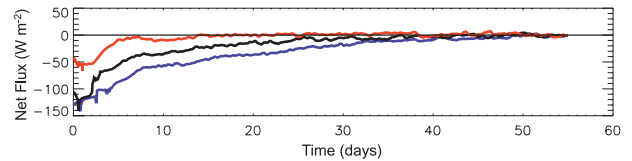


FIG. 1. Time series plots of the difference between total surface (sensible plus latent) heat flux and the net radiative flux for simulations run with fixed SSTs of 298 K (blue), 300 K (black), and 302 K (red).

SST as a lower boundary condition in CRM-based RCE experiments, such experiments are not a perfect analog to climate change experiments in which carbon dioxide concentration increases. This is in large part due to the fact that increased CO_2 leads to additional radiative cooling in the upper troposphere, which can in turn lead to enhancement in the vigor of deep convection. We use present-day concentrations of CO_2 in each of our simulations. Finally, it should be pointed out that use of fixed SSTs does not close the feedback loop from the atmosphere back to the SST that occurs in the real climate system or in coupled ocean–atmosphere GCMs. While we acknowledge the importance of mutual atmosphere–ocean feedbacks, simulation of the fully coupled atmosphere–ocean system is not possible with the current configuration of RAMS.

3. Bulk characteristics of the hydrologic cycle in radiative–convective equilibrium

Table 1 summarizes the mean state of the system in equilibrium over days 45–55 in each of the three experiments described above. Note that in the results that follow, we shall refer to *disturbed* and *undisturbed* regions in the simulated domain, by which we mean regions that exhibit frequent deep convection and those that do not, respectively. For simplicity, we use a threshold on the outgoing longwave radiative (OLR) flux of 260 W m^{-2} to discriminate between the two. We have tested other measures, as well as small changes to the threshold OLR value, and found negligible sensitivity in the results.

Consistent with an increase in the equilibrium vapor pressure with increasing temperature, the mean column-integrated water vapor [hereafter precipitable water (PW)] increases monotonically with sea surface temperature. The total mean precipitation rate also increases, while the domain mean OLR decreases, consistent with an increase in the infrared opacity of the atmosphere with increasing water vapor content and increasing high cloud. Consistent with a decrease in the rate of infrared cooling, the radiatively driven circulation slows with SST, as reflected in a decrease in upward (downward) mass

TABLE 1. Means of cloud, radiation, and vertical mass flux variables averaged over the entire domain and for the last 10 days of each simulation.

	SST		
	298 K	300 K	302 K
Mean PW, full domain (kg m^{-2})	29.34	38.00	48.20
Mean precipitation rate (mm h^{-1})	2.199	2.384	2.485
Mean OLR, full domain (W m^{-2})	245.04	241.27	240.59
High cloud fraction (%)	33.65	36.31	37.41
Mean TWP, full domain (g m^{-2})	96.14	96.54	91.90
Mean LWP, full domain (g m^{-2})	33.81	38.08	38.11
Mean IWP, full domain (g m^{-2})	62.33	58.45	53.79
Mean vertical mass flux: Disturbed regions ($\text{kg m}^{-2} \text{ s}^{-1}$)	0.154	0.125	0.104
Mean vertical mass flux: Undisturbed regions ($\text{kg m}^{-2} \text{ s}^{-1}$)	-0.095	-0.090	-0.076
Mean surface wind speed (m s^{-1})	1.62	1.58	1.33

flux in disturbed (undisturbed) regions, as well as in a decrease in the mean surface wind speed. It is interesting to note that, while the PW increases with SST, the vertically integrated total condensed water (TCW) does not. There is a slight increase in TCW between 298 and 300 K, then a notable decrease between 300 and 302 K. Looking at the contributions to TCW from liquid and ice, we see that the vertically integrated liquid condensate [liquid water path (LWP)] increases between 298 and 300 K, then remains nearly constant from 300 to 302 K. In contrast, there is a monotonic *decrease* in vertically integrated frozen condensate [ice water path (IWP)], which runs counter to recent observational studies that report an increase in upper-tropospheric ice content with increasing SST (e.g., Su et al. 2006). We shall explore the possible reasons for this apparent discrepancy in more detail in section 5.

In addition to an increase in the mean precipitation rate with SST, there is an increase in the convective intensity (Table 2). The mean vertical velocity in convective updrafts (defined by convention as regions with vertical velocity greater than 1 m s^{-1}) increases with

SST, while the fraction of the domain occupied by deep convective cores decreases. The number of columns with very large precipitation rates ($>250 \text{ mm day}^{-1}$) and vertical velocities ($>10 \text{ m s}^{-1}$) also increases with SST. Convective intensity is also reflected in the properties of the low-level thermal perturbation (cold pool) (e.g., Moncrieff and Miller 1976; Thorpe et al. 1982) produced by below-cloud evaporation and/or melting of precipitation. Cold pools by nature are density currents, typically defined via a buoyancy criterion (e.g., Tompkins 2001c). This is appropriate in the study of the convective-scale interaction between cold pools and the environment, however, the grid spacing of our simulations is too coarse to resolve finescale cold pool dynamics. Instead, we consider low-level thermal perturbations associated with deep convection from a bulk perspective. We define cold pools to be regions with a negative surface potential temperature perturbation greater than two standard deviations below the mean. This encompasses regions of relatively intense precipitation and is designed to measure convective intensity by sampling only those grid points directly associated

TABLE 2. As in Table 1 but for statistics describing changes in convective intensity with SST.

	SST		
	298 K	300 K	302 K
Mean w where $w > 1$	2.665	2.906	3.042
Percent of domain with $w > 1 \text{ m s}^{-1}$	1.047%	0.791%	0.783%
Percent of domain with $w > 10 \text{ m s}^{-1}$	0.025%	0.032%	0.039%
Percent of domain with precipitation $> 250 \text{ mm day}^{-1}$	0.197%	0.212%	0.234%
Percent of domain containing cold pools	2.32	3.38	4.83
Mean temperature perturbation in cold pools (K)	-1.12	-1.15	-1.10
Precipitation rate in cold pools (mm h^{-1})	9.01	9.63	10.15
Percent of precipitation falling in cold pools	79.58%	74.87%	86.00%
Mean convective mass flux ($\text{kg m}^{-2} \text{ s}^{-1}$)	4.881	4.085	3.797
Mean stratiform mass flux ($\text{kg m}^{-2} \text{ s}^{-1}$)	0.043	0.030	0.021
Percent of precipitation in convective regions	30.42%	29.18%	35.87%
Percent of precipitation in stratiform regions	66.22%	67.66%	61.06%

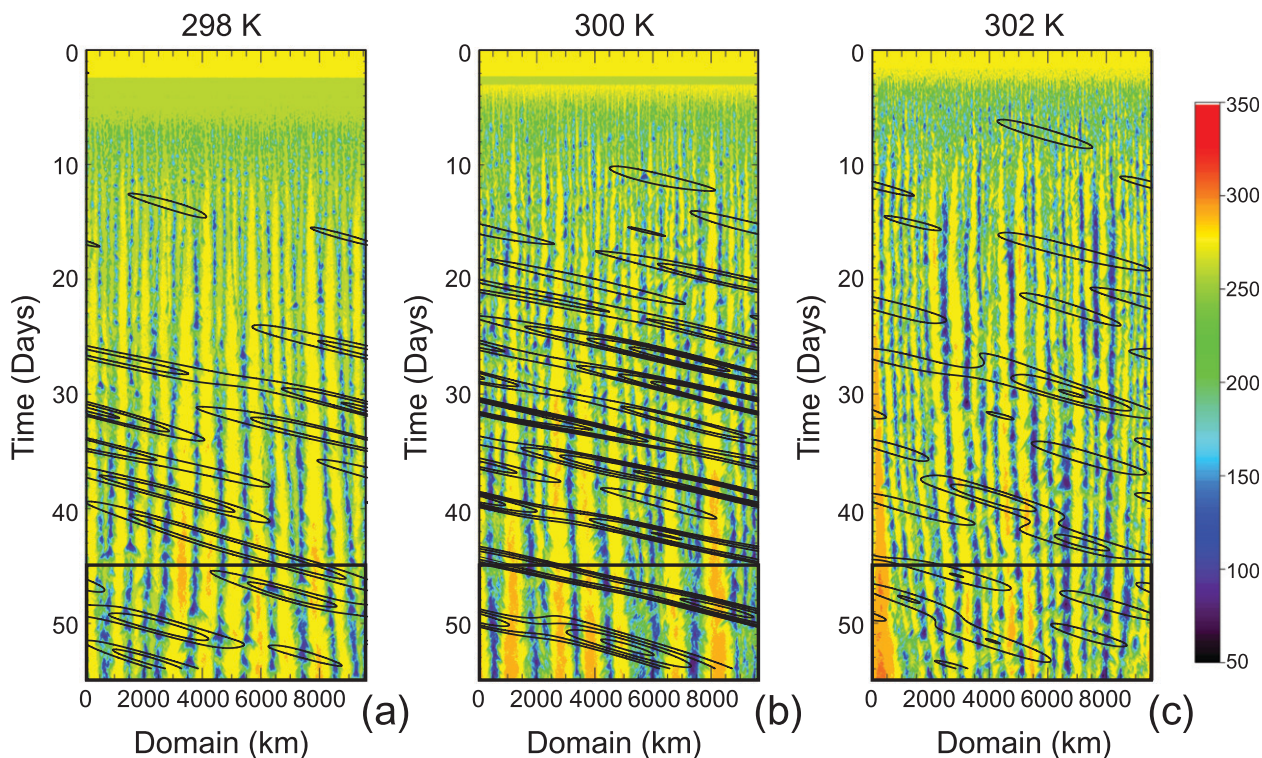


FIG. 2. Hovmöller plots of outgoing longwave radiative flux for simulations run with fixed SSTs of (a) 298 K, (b) 300 K, and (c) 302 K. The black box denotes the 10-day averaging period at the end of each simulation, while black contour lines denote filtered negative OLR anomalies from the portion of the wavenumber–frequency domain that corresponds to equatorial Kelvin waves. OLR anomalies are contoured every 2.5 W m^{-2} with the outermost contour at -2.5 W m^{-2} .

with convectively driven downdrafts. The results (Table 2) indicate a monotonic increase in the cold pool fractional area and attendant increase in precipitation rate within these regions, where the mean cold pool precipitation rate is computed only where precipitation rates exceed 1 mm h^{-1} . Interestingly, though the precipitation rate in cold pools increases with SST, the fraction of precipitation that falls inside a cold pool does not; cold pool precipitation fraction increases between 298 and 302 K, but is lower at 300 K. The fact that the magnitude of the mean temperature perturbation within cold pools is nearly invariant with SST reflects that the low-level relative humidity is also nearly constant with SST, a fact we shall explore in more detail in section 4.

To further examine changes in convective and stratiform precipitation and mass flux, we apply a convective/stratiform partitioning scheme [the so-called Goddard Cumulus Ensemble (GCE) method, Lang et al. 2003]. The results reveal a monotonic decrease in both convective and stratiform vertical mass flux with SST consistent with the decrease in disturbed-region vertical mass flux noted above. Consistent with a decrease in cold pool precipitation fraction at 300 K, there is a slight decrease (increase) in convective (stratiform) precipitation

fraction with transition from 298 to 300 K SST, and a moderate increase (decrease) in convective (stratiform) precipitation fraction between 300 and 302 K. These changes in convective versus stratiform precipitation fraction reflect an apparent transition in the character of convective systems around a SST of 300 K; we will return to this in more detail later.

4. Changes in the large-scale characteristics of convection with SST

a. Large-scale organization

Figure 2 depicts Hovmöller plots of OLR for each simulation averaged over the meridional portion of the domain. Within a few days of model initialization, convection self-aggregates into disturbed and undisturbed regions, with disturbed regions characterized by relatively low values of OLR, whereas undisturbed regions are characterized by relatively high values of OLR. In documenting characteristics of the 300-K simulation, Posselt et al. (2008) showed that disturbed regions also exhibit relatively large values of PW, frequent troposphere-deep convection, and general ascent. Undisturbed regions are characterized by low values of PW, clear air or clouds

with tops well below the freezing level, and general troposphere-deep descent. Similar self-aggregation of convection into large clusters has been noted in studies of observed convective systems in the tropical Pacific (Nakazawa 1988; Mapes 1993; Mapes and Houze 1993), though it is important to note that our simulations are highly idealized and aggregation is not meant to be an exact analog to the observed tropics.

Also apparent in each simulation is the fact that convection in disturbed regions undergoes cyclic changes in intensity. This is reflected in time series of the mean OLR within select disturbed regions (Fig. 3) from which it can be seen that the time between OLR minima is approximately two days. This cyclic variability in OLR appears to be associated with the presence of propagating large-scale waves in the domain. To better illustrate the presence of these waves, we have applied a time-space filtering algorithm to the OLR fields (e.g., Wheeler and Kiladis 1999) and have further subset the filtered results to isolate eastward propagating Kelvin waves. The filtered negative OLR anomalies associated with these waves are highlighted in the thin black lines in the Hovmöller plots of OLR in Fig. 2. These waves have a group velocity of $15\text{--}20\text{ m s}^{-1}$ (increasing with SST), consistent with observations and theoretical studies of equatorial Kelvin waves (e.g., Kiladis et al. 2009), and we will hereafter refer to these waves in our simulations as convectively coupled gravity waves. Similar propagating convectively coupled gravity waves with 2-day periodic convective intensification have been reported in two-dimensional CRM-based RCE simulations (e.g., Grabowski et al. 2000; Tulich et al. 2007). Grabowski et al. attributed the 2-day period to the time necessary for these waves to traverse the length of their 4000-km domain. Our domain is more than twice the width of theirs, yet we observe a similar 2-day period, indicating the recurrence interval of these waves is not governed in our simulations by the domain width. It has been hypothesized in both theoretical and observational studies that this 2-day oscillation is associated with instability in the third baroclinic mode (Yano et al. 2002). We shall revisit evidence for the existence of a third baroclinic mode in our simulations in more detail shortly. Note that convective systems themselves appear to originate near the center of disturbed regions and propagate outward, but do not propagate far into the undisturbed regions between. This is likely due to the fact that, while there is shear near the edges of disturbed regions, there is no domain-mean troposphere-deep mean vertical shear of the horizontal wind. We have conducted limited tests in which a mean shear typical of the west Pacific warm pool region is imposed; these exhibit westward propagating squall-line-type systems.

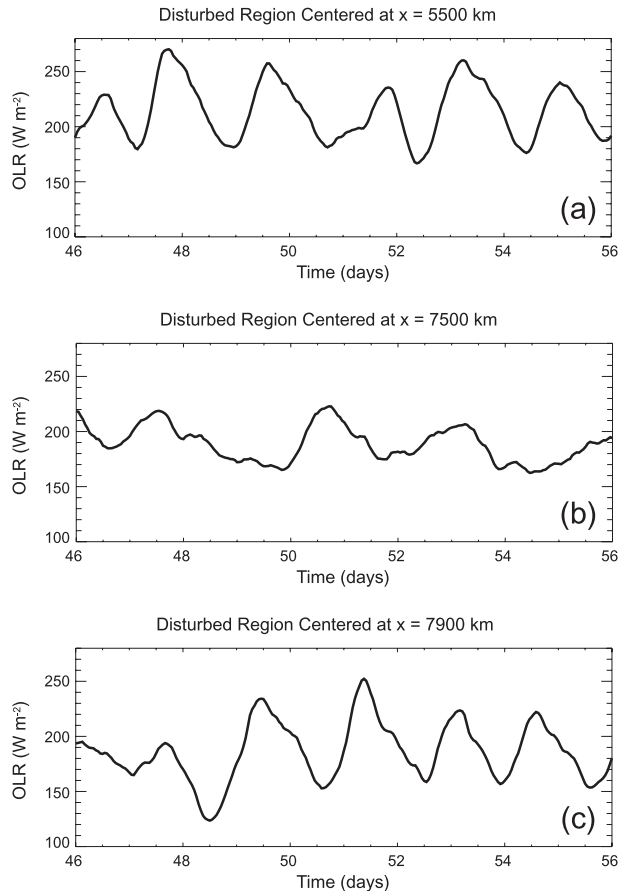


FIG. 3. Time series plots of the mean outgoing longwave radiative flux in select disturbed regions for simulations run with SST of (a) 298 K, (b) 300 K, and (c) 302 K.

The characteristics of the radiatively driven large-scale overturning circulation at RCE can be examined via plots of the mean zonal wind profile between disturbed and undisturbed regions (Fig. 4). To construct these plots, we first examine Hovmöller plots of OLR over the 10 days of interest to identify disturbed regions. For each region, we then define the boundary of each disturbed region to be the position of the 260 W m^{-2} OLR contour that lies farthest from the region center over the 10-day period. Finally, we construct a 10-day mean of the zonal wind across this boundary. Disturbed region-relative winds are composited by defining flow directed into disturbed regions to be negative in sign and flow directed out of disturbed regions to be positive in sign. In these plots, the lower-tropospheric inflow into and upper-tropospheric outflow from disturbed regions is clearly evident, as is the fact that the lower- (upper-) tropospheric inflow (outflow) weakens with increasing SST. This is consistent with the weakening of the mean vertical mass flux in disturbed and undisturbed regions noted previously (Table 1). A similar slowing of the

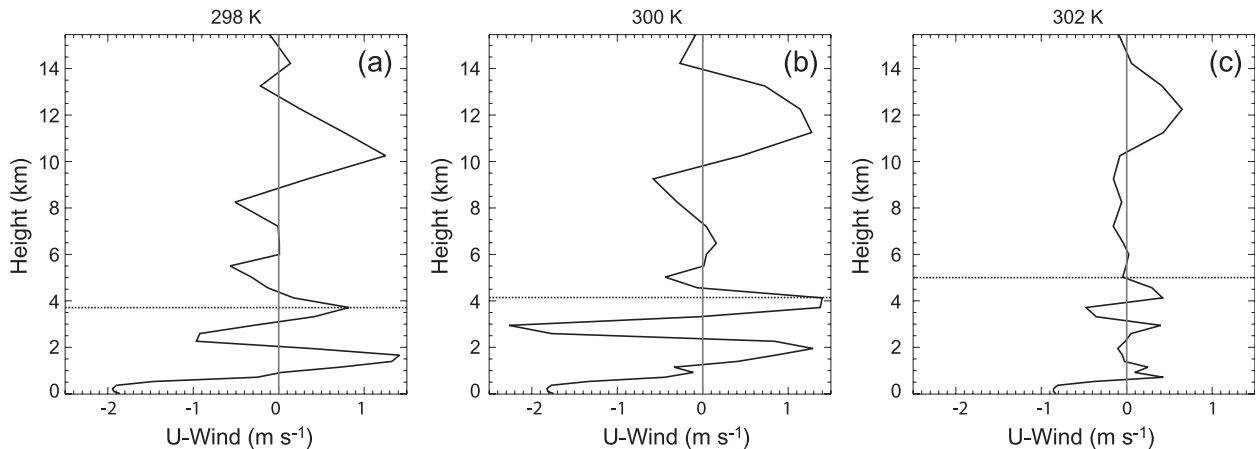


FIG. 4. Vertical profiles of zonal wind relative to the boundaries of disturbed regions corresponding to SST (a) 298 K, (b) 300 K, and (c) 302 K.

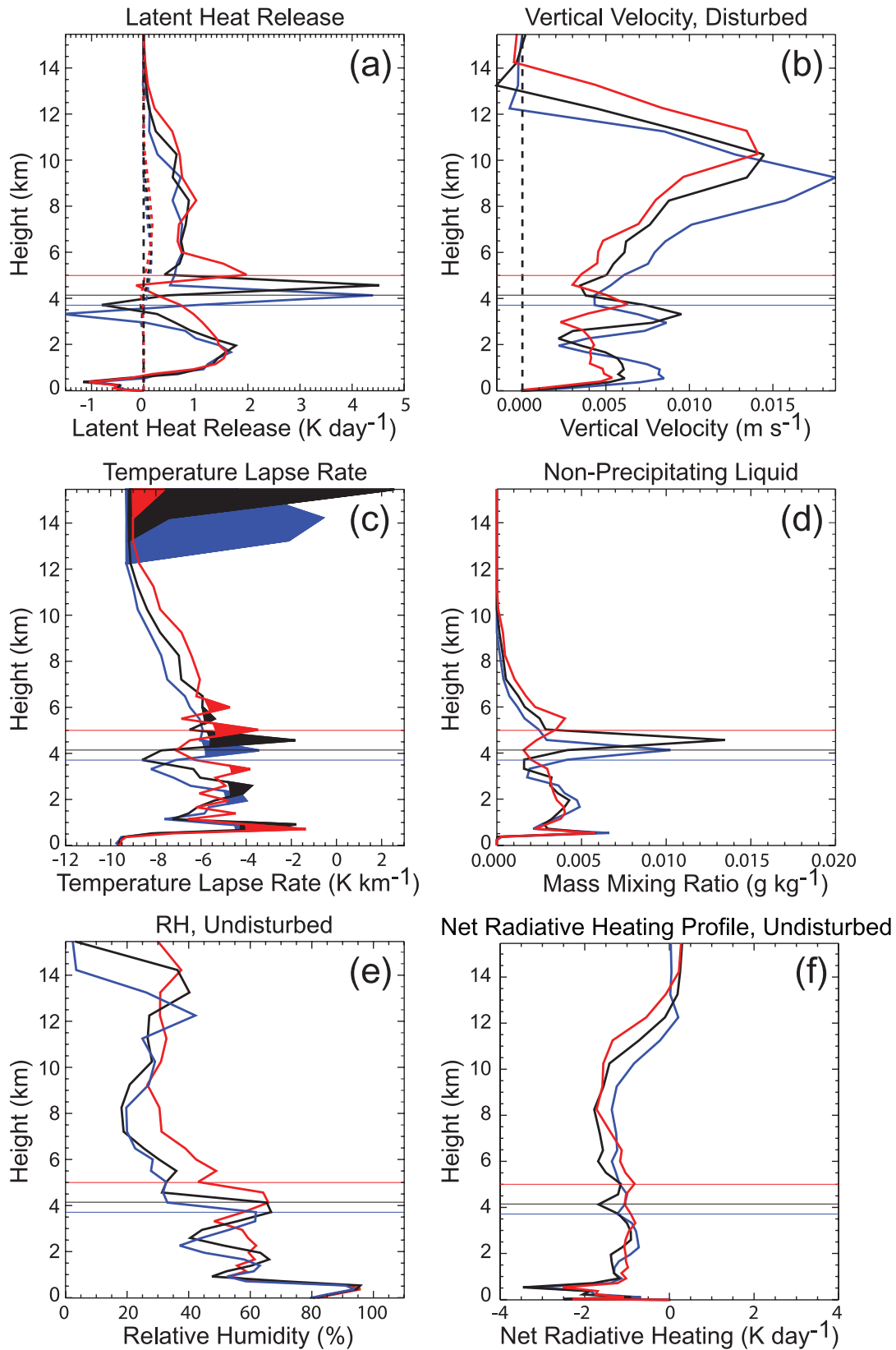
troposphere-deep overturning circulation in the presence of increase in total precipitation has been noted by Held and Soden (2006) in a study based on the suite of coupled climate models used in the Fourth Assessment Report (AR4) of the Intergovernmental Panel on Climate Change (IPCC). They noted that the relatively small changes in radiative flux with increasing tropospheric water vapor content imply a decrease in the rate of exchange of mass between the boundary layer and the midtroposphere, and a consequent weakening of the tropical overturning circulation. Vecchi and Soden (2007) note that the zonal overturning circulation (Walker) cell decreases with increasing surface temperature at a much greater rate than does the meridional (Hadley) cell.

There are clear differences in the vertical structure of the large-scale circulation between 302 K and 298 and 300 K. Lower and middle tropospheric outflow from disturbed regions is present in the 298-K and 300-K simulations at approximately 2 and 4 km above the surface, as well as regions of inflow at approximately 3, 6, and 8 km. These features are noticeably weaker at 302 K, and the outflow at 2 km is notably absent. In addition, whereas there are two regions of midtropospheric inflow into disturbed regions at 298 and 300 K, those at 302 K are much weaker and much deeper. Splitting of the troposphere-deep vertical overturning circulation into two shallower branches is consistent with the results presented by Yano et al. (2002), who used linear stability analysis to examine the interaction between convectively coupled waves and Walker-type overturning circulations. They noted that the first baroclinic mode (corresponding to troposphere-deep ascent and descent) is linearly unstable and quasi-steady. The third baroclinic mode interacts with the troposphere-deep mode, producing quasi-stable oscillations with an approximately 2-day period. Mapes

(2001) notes that troposphere-deep convective heating should be accompanied by midtropospheric divergence from, and upper to middle tropospheric convergence into, regions of organized convection in addition to the canonical lower-tropospheric convergence and upper-tropospheric divergence commonly associated with the tropical large-scale overturning circulation. In his analysis of observed tropical soundings, he also highlights mass exiting regions of convective heating at approximately 1.5 and 4.5 levels above the surface. The vertical profiles of disturbed region-relative wind and 2-day oscillation in convective intensity are broadly consistent with the presence of a prominent third baroclinic mode, and with the theoretical two-celled response to deep convective heating. However, the morphological changes in convective organization (Fig. 2) and large-scale circulation (Fig. 4) with warming SST are striking, and indicative of a transition in the character of convection around sea surface temperatures of 300 K that have also been noted in observation-based studies of tropical convection (Zhang 1993; Masunaga et al. 2005; Su et al. 2006). We will expand on the transition at 300 K in section 5.

b. Changes to convective morphology with increasing SST

Vertical profiles of disturbed-region vertical velocity and latent heat release (LHR) are depicted in Figs. 5a and 5b. Notable in both plots are the large values of latent heat release and upward vertical velocity present in the midtroposphere. The plot of the domain-mean mixing ratio of nonprecipitating liquid (Fig. 5c) indicates that this spike in LHR is associated with the conversion of water vapor to liquid cloud associated with vertical convergence of mass in the midtroposphere. This vertical mass convergence is likely what is driving the strong



midlevel flow out of disturbed regions noted in the previous section (Fig. 4). Comparison of the mean vertical profile of temperature lapse rate with the moist adiabatic lapse rate (Fig. 5d) reveals the presence of a significant midtropospheric stable layer just above the freezing level. This stable layer lies just atop the region of enhanced condensational heating, while the maximum in vertical velocity lies under the stable layer in a region of decreased static stability. Detrainment of condensate from regions of organized convection is reflected in the maximum in relative humidity observed just below the stable layer (Fig. 5e), and profiles of net radiative heating reveal a local maximum in net radiative cooling at the top of the midtropospheric moist layer at 298 and 300 K (Fig. 5f). While a complete exploration of the mechanisms that lead to the formation and maintenance of the freezing-level stable layer is beyond the scope of this study, such a stable layer has been commonly observed over the tropical oceans (Johnson et al. 1996; Mapes 2001; Yasunaga et al. 2006; Posselt and Charboneau 2011, manuscript submitted to *J. Geophys. Res.*), as has a midtropospheric maximum in stratiform cloudiness (Yasunaga et al. 2006; Posselt and Charboneau 2011, manuscript submitted to *J. Geophys. Res.*). It has been hypothesized that this stable layer is formed by melting of frozen precipitation in the stratiform regions of convective systems, though radiative cooling has also been offered as an explanation for its persistence (Posselt et al. 2008). To examine the possibility that melting is the cause of this stable layer in our RCE simulations, we partitioned latent heat release into a portion associated with vapor to liquid or ice phase change and a portion associated with freezing and melting (Fig. 5a). Melting-induced latent heat release is indeed concentrated just below the freezing level, but is very small compared to the latent heat of condensation within the freezing layer (cf. maximum of -0.05 K day^{-1} mean melting rate with maximum of 4.5 K day^{-1} for condensation). In addition, it is important to note that a melting-induced stable layer should form just *below* the freezing level, while the stable layer in our simulations forms immediately *above* it.

The fact that the stable layer is located in close proximity to the freezing level potentially implicates the freezing/melting process in its initial formation, but at RCE

the feature appears to be maintained and reinforced by a combination of a vertical gradient in radiative cooling and a buoyancy-driven circulation in the lower troposphere. In this case, buoyancy-driven vertical motion in the lower troposphere impinges on the stable layer leading to vertical moisture convergence and condensation. The consequent maximum in latent heating within the stable layer in turn leads to lateral gravity wave propagation and subsidence induced heating. This subsidence acts on detrained condensate at midtropospheric levels leading to evaporation and associated cooling along with a maximum in relative humidity just below the freezing level. A vertical gradient in radiative cooling at the top of the moist layer leads to a relatively greater cooling rate at the base of the stable layer. The combination of subsidence-induced heating above with evaporation- and radiation-induced cooling below leads to the maintenance of a strong stable layer located just above the freezing level. It should be noted that, in simulations without mean vertical wind shear, convective systems do not propagate out of disturbed regions, and the thermal structure in regions of large-scale descent is left undisturbed for long periods of time. In reality, propagating convective systems thoroughly mix the atmosphere throughout the depth of the troposphere, and observed stable layers are much weaker than those in our simulations (Posselt and Charboneau 2011, manuscript submitted to *J. Geophys. Res.*).

The analysis presented above reveals a monotonic increase in convective intensity with increasing SST as measured by both the precipitation rate and convective updraft speed, as well as by the expansion of (and increase in precipitation rate in) convective cold pools. Increases in convective intensity occur in the context of a weakening in the large-scale overturning circulation. Interestingly, both the large-scale circulation and convective-system-scale results demonstrate a change in the nature of convection around the 300-K SST noted in previous studies (Zhang 1993; Masunaga et al. 2005; Su et al. 2006), and we offer a more detailed analysis of the possible mechanisms behind this transition in the next section.

5. On the transition around 300 K

Transition to strong convection in the tropics has been hypothesized to involve preconditioning of the middle

←

FIG. 5. Vertical mean profiles of domain-mean (a) latent heat release associated with vapor to liquid/ice (solid lines) and freezing/melting (dashed lines) processes, (b) vertical velocity in disturbed regions, (c) temperature lapse rate, (d) nonprecipitating liquid condensate, (e) undisturbed region relative humidity, and (f) net radiative cooling rate averaged over the last 10 days of each simulation. Horizontal lines denote the freezing level in each simulation, and blue, black, and red lines correspond to SST values of 298 K, 300 K, and 302 K, respectively.

TABLE 3. As in Table 1 but for three layer relative humidity, liquid water path, and ice water path.

	SST		
	298 K	300 K	302 K
RH* low	73.94	73.36	73.40
RH* mid	50.60	55.40	57.40
RH* high	32.10	33.47	39.11
Mean LWP, lower troposphere	17.91	23.17	25.93
Mean LWP, midtroposphere	15.32	14.39	11.75
Mean LWP, upper troposphere	0.58	0.52	0.44
Mean IWP, lower troposphere	0.07	0.15	0.08
Mean IWP, midtroposphere	18.38	17.73	16.00
Mean IWP, upper troposphere	43.88	40.56	37.72
Mean IWP, upper troposphere (400 hPa < P < 100 hPa)	34.40	35.17	37.72

troposphere by developing convective cores. Moistening of the atmosphere by convection can be assessed by examining changes in the saturation fraction (RH*) (Bretherton et al. 2004) with SST. Because we wish to examine moistening of the lower, middle, and upper troposphere separately, we compute a layer saturation fraction defined as the layer PW divided by the layer-saturated PW. If we wish to properly describe changes in the thermodynamic environment consistent with changes in cloud system characteristics, we must account for the fact that the height of both the freezing level and the tropopause increase with SST. Hence, we define the boundaries between layers dynamically such that the lowest layer extends from the surface to 1 km below the freezing level, the middle layer from 1 km below to 2 km above the freezing level, and the upper layer from 2 km above the freezing level to the tropopause. We contend that layers thus defined better represent the influence of convection on the lower, middle, and upper troposphere than static layers, and allow a more robust examination of moistening of low levels and boundary layer venting, midtropospheric preconditioning, and the moistening of the upper troposphere due to detrainment of vapor and condensate from deep convection. Examination of the three-layer RH* (Table 3) reveals a near-constant low-level saturation fraction with SST, consistent with the near-constant temperature perturbation in convective cold pools. Midtropospheric saturation fraction exhibits a larger increase between 298–300 K relative to 300–302 K, while the upper-tropospheric saturation fraction increases only slightly from 298 to 300 K, with a much larger increase from 300 to 302 K. If we examine the changes to LWP and IWP in these three layers, we see a monotonic increase in LWP in the lowest layer with a steady decrease in the middle troposphere. IWP decreases monotonically in both the middle and upper troposphere. It is interesting to note that, if we instead define lower, middle, and upper layers based on constant pressure levels (e.g., compute upper-tropospheric

IWP in the 100–400-hPa layer at each SST), the IWP appears to increase with SST.

To isolate the characteristics and frequency of shallow and deep convection from stratiform cloud, we apply a cloud partitioning scheme to the model results. Partitioning is motivated by the well-observed trimode spectrum of clouds in regions of frequent deep convection (Johnson et al. 1999; Kikuchi and Takayabu 2004; Haynes and Stephens 2007). We adopt a four-class partitioning scheme (Table 4) based on observations of the structure of mesoscale convective systems in the tropics (e.g., Houze 2004), and described in detail in Tulich et al. (2007, hereafter TRM07). Following TRM07, we divide clouds into shallow convection, deep convection, and stratiform; however, our scheme differs from that of TRM07 in that we use the dynamic definitions of low-, middle, and upper-tropospheric layers presented at the beginning of this section. In addition, we further subdivide stratiform cloud using a threshold precipitation rate of 1 mm day^{-1} to discriminate between precipitating and nonprecipitating clouds.

Examination of the results of the four-class partitioning scheme reveals a monotonic decrease in the fraction of the domain classified as either shallow or deep convection along with an increase in the shallow and deep convective precipitation rate, reflecting a general decrease in the frequency of convection, but an increase in intensity where it does occur. Interestingly, the fraction of shallow convection is much larger than the fraction of deep convection and approximately two times the frequency of precipitating stratiform, but the precipitation rate is two orders of magnitude less. This reflects the fact that, in contrast to other convective–stratiform partitioning methods (e.g., the GCE scheme used above in Table 2 and documented in Lang et al. 2003), precipitation at the surface is not a prerequisite for classification of a column as convective. Since model grid spacing is not fine enough to resolve shallow convective cores (e.g., congestus clouds), our scheme is instead

TABLE 4. As in Table 1 but for results of the four-class partitioning scheme.

	SST		
	298 K	300 K	302 K
Percent deep convective cores	0.732	0.719	0.693
Percent shallow convective	6.113	5.767	5.015
Percent precipitating stratiform	2.987	3.758	2.804
Percent nonprecipitating stratiform	25.645	28.513	29.212
Deep convective precipitation rate	210.848	232.255	269.543
Shallow convective precipitation rate	2.406	3.038	3.707
Precipitating stratiform precipitation rate	18.588	15.965	17.760
Deep convective precipitation fraction	68.025	67.797	72.727
Shallow convective precipitation fraction	6.520	7.127	7.272
Precipitating stratiform precipitation fraction	24.241	24.126	19.426
Deep convective vertical velocity (cloudy, $w > 0$)	0.842	0.821	0.900
Shallow convective vertical velocity (cloudy, $w > 0$)	0.089	0.099	0.105
Precipitating stratiform vertical velocity (cloudy, $w > 0$)	0.132	0.113	0.128
Stratiform vertical velocity (cloudy, $w > 0$)	0.107	0.097	0.098

keying in on developing (and largely weakly precipitating) convection at lower and middle tropospheric levels. As such, the statistics for what TRM07 refer to as shallow convection are representative of the effect of these clouds on the midtropospheric environment. It is interesting to note that the vertical velocity in and fraction of precipitation from shallow convection increases monotonically with SST, while deep convective vertical velocity and precipitation fraction are lower at 300 K relative to 298 and 302 K. The fraction of the domain containing precipitating stratiform cloud is higher at 300 K than at 298 and 302 K while the mean precipitation rate is lower, resulting in nearly an identical fraction of the total precipitation produced by stratiform cloud at 298 and 300 K. It is notable that the fraction of the total precipitation from stratiform cloud decreases from 300 to 302 K; accordingly, the total convective (shallow + deep) precipitation fraction is nearly equivalent at 298 and 300 K and increases with transition to 302 K.

Our results highlight the importance of preconditioning of the middle troposphere by shallow convection, noted in previous studies, but also indicate a secondary role for shallow convection. In addition to moistening the middle troposphere such that the effect of entrainment on buoyancy is reduced, shallow convection also helps to overcome the inhibition associated with the midlevel stable layer. With an increase in sea surface temperature to 300 K, the increase in low-level water vapor and increase in lower-tropospheric buoyancy support an increase in shallow convection, while deep convection remains suppressed by the midlevel stable layer and a relatively dry upper troposphere. Mixing between deep convection and the environment limits the frequency of deep convection when the upper troposphere is dry. In our simulations, this reduction in deep convective

buoyancy is reflected in a decrease in convective updraft speed and fraction of total precipitation with the increase in SST from 298 to 300 K.

In the final component of our analysis, we examine the relationship between precipitation rate and PW. Changes in convective precipitation rate with increasing PW has been hypothesized to operate as a continuous phase transition, with a transition to strong convection and precipitation above a critical value of PW (Peters and Neelin 2006; Neelin et al. 2009, hereafter NPH09). Following NPH09, we compute the mean and variance of the precipitation rate for each simulation in 0.3-mm PW bins (Figs. 6a and 6b). As in NPH09, we note a rapid pickup in precipitation rate and precipitation rate variance with increasing PW; however, while NPH09 show saturation of precipitation rate and precipitation rate variance at PW values above criticality, our simulations exhibit an increase in scatter. This reflects the fact that, at large PW values, the precipitation rate is a function not only of the atmospheric water vapor content, but also of the surface wind speed and the mesoscale organization of convection (Back and Bretherton 2005; Raymond et al. 2009). Based on the location of the increase in scatter in each plot, we obtain transition PW values of approximately 46, 57, and 70 mm for SSTs of 298, 300, and 302 K, respectively. The troposphere mean temperature (defined between 1000 and 200 hPa as in NPH09) for each run is approximately 264, 269, and 273 K, respectively, and our results are generally consistent with those obtained by NPH09 (e.g., their Fig. 1a).

Along with the binned precipitation, we also examine histograms of PW in the full domain (Fig. 6c) and for regions in which the precipitation rate exceeds 1 mm h^{-1} (Fig. 6d). The shape of the histogram of PW in precipitating regions is consistent across all simulations,

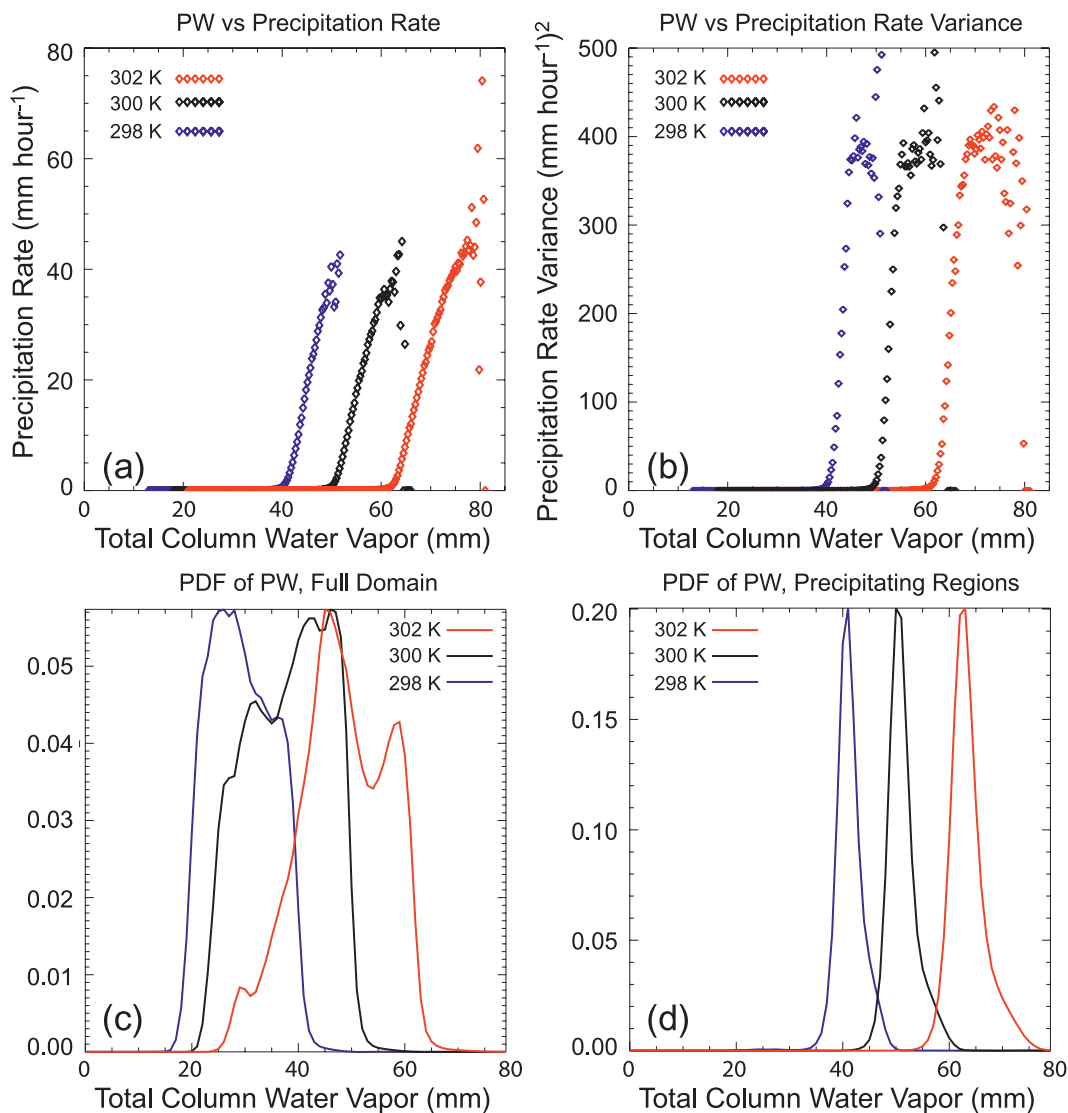


FIG. 6. (a) Mean precipitation rate and (b) variance, binned in 0.3 kg m^{-2} intervals of PW. (bottom) Histograms of PWV over (c) the full domain and (d) only in regions with precipitation rate greater than 1 mm h^{-1} . All data is from the last 10 days of each simulation, and in each plot, blue, black, and red lines correspond to SST values of 298 K, 300 K, and 302 K, respectively.

with a mode that peaks just above the critical value and with a tail toward larger values of PW. However, the histograms of PW over the full domain exhibit notable differences. At 298 and 302 K, the mode of the histogram (e.g., PW value that occurs most frequently in the domain) is located well below the critical value. This reflects the fact that undisturbed regions occupy a large portion of the domain and that the characteristics of disturbed regions are distinct from those of undisturbed regions. However, though there is distinct peak in the PW at low values in the 300-K simulation, the majority of the columns exhibit PW values relatively close to the critical value. The increasing prevalence of columns with

near (but sub-) critical PW at SST of 300 K is consistent with the greater amount of stratiform cloud relative to convective in the four-class partitioning scheme above.

Recall that the notion of a critical value of PW arises from the idea that water vapor slowly accumulates in the tropical troposphere until the onset of convective precipitation, which increases in intensity in a power-law relationship with PW above criticality. In stratiform regions (which in the tropics are nearly uniformly associated with deep convection), the mean dissipation (precipitation) rate is an order of magnitude smaller than the mean rate in convective regions. The PW histograms, along with the results of stratiform/convective cloud partitioning, hint

at a change in the interaction between cloud systems and the environment around a 300-K SST in which the removal of water vapor in precipitating regions occurs at a slower rate than at 298 and 302 K. At 300 K the dry upper troposphere and strong midlevel stable layer act to inhibit deep convection. Stratiform precipitation is relatively more frequent and acts to remove water vapor from the atmosphere, but the rate of removal is much slower than that of deep convection and the domainwide PW values remain relatively close to the critical value.

6. Conclusions

In this paper we have examined the effect of warming sea surface temperatures on the interaction of deep convective cloud systems with both the near-field and far-field environment. Our experiments employed large-domain cloud-system-resolving simulations run to a state of radiative–convective equilibrium at fixed sea surface temperatures of 298, 300, and 302 K. Examination of the energy budget and bulk hydrological cycle revealed that the rate of increase in atmospheric water vapor content is not governed solely by the characteristics of the surface but is, instead, sensitive to the vertical structure of the atmospheric warming and that this vertical structure is in turn influenced by the effects of convection on its surrounding environment. Our major findings include the following:

- Several measures of the large-scale rate of overturning and convective intensity reveal a slowing in the large-scale circulation and increase in convective intensity with increasing SST. However, there is a transition in the behavior of convection and the interaction with the environment around 300-K SST. This transition can be clearly seen in the increase in the fraction of stratiform precipitation and decrease in convective vertical mass flux at 300 K relative to 298 and 302 K, as well as in the changes in vertical structure of condensate, latent heat release, and the vertical profile of flow into and out of regions of organized convection.
- Examination of the lower-, middle-, and upper-tropospheric saturation fraction, LWP, and IWP reveals a near-constant low-level saturation fraction, with a notable increase in middle-tropospheric RH* from 298 to 300 K and an increase in upper-level RH* from 300 to 302 K. These increases are concurrent with a decrease in the total and upper-tropospheric IWP, though we note that, if we define the upper troposphere based on constant pressure levels, the IWP appears to increase with SST.
- Partitioning clouds into deep convective, shallow convective, and stratiform reveals a monotonic increase in the vigor of shallow convection with SST, while deep convective vertical velocity is lower at 300 K relative to the 298-K and 302-K simulations.
- Examination of the vertical structure of condensate, LHR, and the environmental static stability profile reveals a strong stable layer located just above the freezing level at 298 and 300 K and at the freezing level at 302 K. There is a sharp decrease in vertical velocity with height just below the freezing level associated with outflow from convectively active regions, and a maximum in non-precipitating liquid condensate and spike in LHR within the stable layer itself. All of these features are weaker in the 302-K simulation than at 298 and 300 K. When considered together, these features hint at a self-reinforcing interaction between convection and the environment at a SST of 298 and 300 K, in which vertical convergence in the freezing-level stable layer leads to a vertically narrow region of large LHR. In the absence of planetary rotation, gravity waves produced by this local heat source induce subsidence and warming outside of actively convecting regions, followed by evaporation of detrained condensate and associated cooling immediately below the freezing level. Troposphere-deep subsidence in the undisturbed region should act to weaken the stable layer, while the combination of subsidence induced by gravity waves and evaporation of detrained condensate appears to strengthen and maintain it.
- Analysis of the precipitation rate and variance, binned by values of PW, reveals our simulations to be consistent with observations of columns with similar values of tropospheric mean temperature. The analysis also shows the 298-K and 302-K simulations to have PW much less than the critical value over most of the domain, while at 300 K, the majority of the columns have near- (but sub-) critical values of PW. We speculate that, at SSTs of 298 and 300 K the dry upper troposphere and strong midlevel stable layer act to inhibit deep convection. Under a scenario of relatively large convective inhibition at 300 K, stratiform precipitation is relatively more frequent and acts to remove water vapor from the atmosphere at a rate much smaller than that of deep convection, leading to domain-mean PW values that remain relatively close to the critical value.

The bottom line is that increasing surface entropy with SST (e.g., Emanuel et al. 1994) should lead to an increase in deep convective intensity, and it does if we consider the per-updraft precipitation rate and vertical velocity. However, a relatively dry upper troposphere and strong midtropospheric stable layer lead to an increase in convective inhibition and decrease (increase) in the fraction of convective (stratiform) precipitation as the SST warms to 300 K. This is reflected in the fact

that PW is close to critical over most of the domain at 300 K and in the increase in the frequency of stratiform precipitation relative to convective. An increase in the vigor of convection below the freezing layer with SST, and the associated moistening of the midtroposphere eventually lead to erosion of the midtropospheric stable layer and increased deep convective precipitation fraction and updraft intensity, reflected in the weaker stable layer and moist upper troposphere at 302 K.

What emerges is the idea of a deep convection rate limiter, active at SSTs up to approximately 300 K, composed of the dual action of a self-reinforcing midtropospheric stable layer and dry upper troposphere. The increase in midtropospheric RH* provided by shallow convection below the freezing level appears to lead to weakening of these limitations by first decreasing the convective inhibition provided by the stable layer then moistening the dry upper troposphere. The combination of more intense deep convection with a moistening upper troposphere at SSTs greater than 300 K suggests the possibility of a positive feedback, but one that manifests as a nonmonotonic function of SST and is dependent on the characteristics of the environment and on the details of the interaction between deep convection and the free troposphere.

In closing, several features in our simulations bear close resemblance to descriptions of the equatorial tropics obtained from theory and observations (e.g., convectively coupled waves, critical values of PW, and the thermal structure of the free troposphere). The geometry of our experiments allowed us to examine changes in deep convective structure and its interaction with the environment on a wide range of scales. That said, our simulations constitute a single (and highly idealized) realization of tropical radiative–convective equilibrium. In addition, the horizontal and vertical resolution of our model is too coarse to explore many of the interesting processes from anything more than a bulk perspective. Questions of the development of the freezing level stable layer, interaction of cold pools, and the role of shallow convection, as well as how all of these respond to warming of the surface and environment, require experiments with far finer horizontal resolution. We leave examination of these questions for future study.

In addition, one of the strengths of the RCE framework exploited in this study is that a fixed SST allows us to examine the response of the atmosphere to surface warming. However, as noted earlier in section 2, this is also a limitation since the real World Ocean responds to changes in the atmospheric temperature and amount of solar and infrared radiative flux. It is impossible (due to the nonlinearity inherent in the interaction between clouds, radiation, and surface properties) to determine a priori how the ocean might respond in each of our

experiments if SST were allowed to vary. For example, the increase in high cloud fraction between SSTs of 298 and 302 K is associated with a decrease in downwelling shortwave radiation at the surface (not shown), which would imply cooling of the upper ocean and a negative feedback in a manner hypothesized by Ramanathan and Collins (1991). However, the decrease in mean surface wind speed with SST leads to a decrease in the wind-generated influence of evaporation, a consequently smaller increase in surface latent heat release between 298 and 302 K, and the possibility of a positive feedback. It may be possible to deconvolve the interaction between competing influences by running RCE simulations with an interactive ocean. We reserve examination of the atmosphere–ocean interaction for future work.

Acknowledgments. This work was supported by the NASA MAP program under Grants NNX08AF77G and NNX09AJ43G. Two anonymous reviewers provided constructive commentary and their critique led to significant improvements in the structure of the manuscript.

REFERENCES

- Back, L., and C. S. Bretherton, 2005: The relationship between wind speed and precipitation in the Pacific ITCZ. *J. Climate*, **18**, 4317–4328.
- Bellon, G., and A. H. Sobel, 2010: Multiple equilibria of the Hadley circulation in an intermediate-complexity axisymmetric model. *J. Climate*, **23**, 1760–1778.
- Bretherton, C. S., M. E. Peters, and L. E. Back, 2004: Relationships between water vapor path and precipitation over the tropical oceans. *J. Climate*, **17**, 1517–1528.
- , P. N. Blossey, and M. Khairoutdinov, 2005: An energy-balance analysis of deep convective self-aggregation above uniform SST. *J. Atmos. Sci.*, **62**, 4273–4292.
- Bryan, G. H., J. C. Wyngaard, and J. M. Fritsch, 2003: Resolution requirements for the simulation of deep moist convection. *Mon. Wea. Rev.*, **131**, 2394–2416.
- Cotton, W. R., and Coauthors, 2003: RAMS 2001: Current status and future directions. *Meteor. Atmos. Phys.*, **82**, 5–29.
- Emanuel, K. A., J. D. Neelin, and C. S. Bretherton, 1994: On large-scale circulations in convecting atmospheres. *Quart. J. Roy. Meteor. Soc.*, **120**, 1111–1143.
- Grabowski, W. W., J.-I. Yano, and M. W. Moncrieff, 2000: Cloud resolving modeling of tropical circulations driven by large-scale SST gradients. *J. Atmos. Sci.*, **57**, 2022–2039.
- Harrington, J. Y., T. Reisin, W. R. Cotton, and S. M. Kreidenweis, 1999: Cloud resolving simulations of Arctic stratus: Part II: Transition-season clouds. *Atmos. Res.*, **51**, 45–75.
- Haynes, J. M., and G. L. Stephens, 2007: Tropical oceanic cloudiness and the incidence of precipitation: Early results from CloudSat. *Geophys. Res. Lett.*, **34**, L09811, doi:10.1029/2007GL029335.
- Held, I. M., and B. J. Soden, 2006: Robust responses of the hydrological cycle to global warming. *J. Climate*, **19**, 5686–5699.
- Houze, R. A., Jr., 2004: Mesoscale convective systems. *Rev. Geophys.*, **42**, RG4003, doi:10.1029/2004RG000150.

- Johnson, R. H., P. E. Ciesielski, and K. A. Hart, 1996: Tropical inversions near the 0°C level. *J. Atmos. Sci.*, **53**, 1838–1855.
- , T. M. Rickenbach, S. A. Rutledge, P. E. Ciesielski, and W. H. Schubert, 1999: Trimodal characteristics of tropical convection. *J. Climate*, **12**, 2397–2418.
- Kikuchi, K., and Y. N. Takayabu, 2004: The development of organized convection associated with the MJO during TOGA COARE IOP: Trimodal characteristics. *Geophys. Res. Lett.*, **31**, L10101, doi:10.1029/2004GL019601.
- Kiladis, G. N., M. C. Wheeler, P. T. Haertel, and K. H. Straub, 2009: Convectively coupled equatorial waves. *Rev. Geophys.*, **47**, RG2003, doi:10.1029/2008RG000266.
- Kuang, Z., and D. L. Hartmann, 2007: Testing the fixed anvil temperature hypothesis in a cloud-resolving model. *J. Climate*, **20**, 2051–2057.
- Lang, S., W.-K. Tao, J. Simpson, and B. Ferrier, 2003: Modeling of convective–stratiform precipitation processes: Sensitivity to partitioning methods. *J. Appl. Meteor.*, **42**, 505–527.
- Mapes, B. E., 1993: Gregarious tropical convection. *J. Atmos. Sci.*, **50**, 2026–2037.
- , 2001: Water's two height scales: The moist adiabat and the radiative troposphere. *Quart. J. Roy. Meteor. Soc.*, **127**, 2353–2366.
- , and R. A. Houze Jr., 1993: Cloud clusters and superclusters over the oceanic warm pool. *Mon. Wea. Rev.*, **121**, 1398–1416.
- Masunaga, H., T. S. L'Ecuyer, and C. D. Kummerow, 2005: Variability in the characteristics of precipitation systems in the tropical Pacific. Part I: Spatial structure. *J. Climate*, **18**, 823–840.
- Moncrieff, M. W., 2004: Analytic representation of the large-scale organization of tropical convection. *J. Atmos. Sci.*, **61**, 1521–1538.
- , and M. J. Miller, 1976: Dynamics and simulation of a tropical cumulonimbus and squall lines. *Quart. J. Roy. Meteor. Soc.*, **102**, 373–394.
- Nakazawa, T., 1988: Tropical superclusters within intraseasonal variations over the western Pacific. *J. Meteor. Soc. Japan*, **66**, 823–839.
- Neelin, J. D., O. Peters, and K. Hales, 2009: The transition to strong convection. *J. Atmos. Sci.*, **66**, 2367–2384.
- Pakula, L., and G. L. Stephens, 2009: The role of radiation in influencing tropical cloud distributions in a radiative–convective equilibrium cloud-resolving model. *J. Atmos. Sci.*, **66**, 62–76.
- Peters, O., and D. Neelin, 2006: Critical phenomena in atmospheric precipitation. *Nat. Phys.*, **2**, 393–396, doi:10.1038/Nphys314.
- Pielke, R. A., and Coauthors, 1992: A comprehensive meteorological modeling system RAMS. *Meteor. Atmos. Phys.*, **49**, 69–91.
- Posselt, D. J., S. C. van den Heever, and G. L. Stephens, 2008: Trimodal cloudiness and tropical stable layers in simulations of radiative convective equilibrium. *Geophys. Res. Lett.*, **35**, L08802, doi:10.1029/2007GL033029.
- Ramanathan, V., and W. Collins, 1991: Sensitivity studies using a cloud-resolving model simulation of the tropical west Pacific. *Quart. J. Roy. Meteor. Soc.*, **117**, 2287–2306.
- Rapp, A. D., C. Kummerow, W. Berg, and B. Griffith, 2005: An evaluation of the proposed mechanism of the adaptive infrared iris hypothesis using TRMM VIRS and PR measurements. *J. Climate*, **18**, 4185–4194.
- Raymond, D. J., S. Sessions, A. Sobel, and Z. Fuchs, 2009: The mechanics of gross moist stability. *J. Adv. Model. Earth Syst.*, **1** (9), doi:10.3894/JAMES.2009.1.9. [Available online at <http://james.agu.org/index.php/JAMES/article/view/v1n9>.]
- Rondanelli, R., and R. S. Lindzen, 2008: Observed variations in convective precipitation fraction and stratiform area with sea surface temperature. *J. Geophys. Res.*, **113**, D16119, doi:10.1029/2008JD010064.
- Saleeby, S. M., and W. R. Cotton, 2004: A large-droplet mode and prognostic number concentration of cloud droplets in the Colorado State University Regional Atmospheric Modeling System (RAMS). Part I: Module descriptions and supercell test simulations. *J. Appl. Meteor.*, **43**, 182–195.
- Sherwood, S. C., and R. Wahrlich, 1999: Observed evolution of tropical deep convective events and their environment. *Mon. Wea. Rev.*, **127**, 1777–1795.
- Sobel, A. H., G. Bellon, and J. Bacmeister, 2007: Multiple equilibria in a single-column model of the tropical atmosphere. *Geophys. Res. Lett.*, **34**, L22804, doi:10.1029/2007GL031320.
- Stephens, G. L., 2005: Cloud feedbacks in the climate system: A critical review. *J. Climate*, **18**, 237–273.
- , S. C. van den Heever, and L. Pakula, 2008: Radiative–convective feedbacks in idealized states of radiative–convective equilibrium. *J. Atmos. Sci.*, **65**, 3899–3916.
- Su, H., W. G. Read, J. H. Jiang, J. W. Waters, D. L. Wu, and E. J. Fetzer, 2006: Enhanced positive water vapor feedback associated with tropical deep convection: New evidence from Aura MLS. *Geophys. Res. Lett.*, **33**, L05709, doi:10.1029/2005GL025505.
- Thorpe, A. J., M. J. Miller, and M. W. Moncrieff, 1982: Two-dimensional convection in non constant shear: A model of midlatitude squall lines. *Quart. J. Roy. Meteor. Soc.*, **108**, 739–762.
- Tompkins, A. M., 2000: The impact of dimensionality on long-term cloud-resolving model simulations. *Mon. Wea. Rev.*, **128**, 1521–1535.
- , 2001a: Organization of tropical convection in low vertical wind shears: The role of water vapor. *J. Atmos. Sci.*, **58**, 529–545.
- , 2001b: On the relationship between tropical convection and sea surface temperature. *J. Climate*, **14**, 633–637.
- , 2001c: Organization of tropical convection in low vertical wind shears: The role of cold pools. *J. Atmos. Sci.*, **58**, 1650–1672.
- , and G. C. Craig, 1998a: Radiative-convective equilibrium in a three-dimensional cloud-ensemble model. *Quart. J. Roy. Meteor. Soc.*, **124**, 2073–2097.
- , and —, 1998b: Time-scales of adjustment to radiative-convective equilibrium in the tropical atmosphere. *Quart. J. Roy. Meteor. Soc.*, **124**, 2693–2713.
- Tulich, S. N., D. A. Randall, and B. E. Mapes, 2007: Vertical-mode and cloud decomposition of large-scale convectively coupled gravity waves in a two-dimensional cloud-resolving model. *J. Atmos. Sci.*, **64**, 1210–1229.
- Vecchi, G. A., and B. J. Soden, 2007: Global warming and the weakening of the tropical circulation. *J. Climate*, **20**, 4316–4340.
- Walko, R. L., and Coauthors, 2000: Coupled atmosphere–biophysics–hydrology models for environmental modeling. *J. Appl. Meteor.*, **39**, 931–944.
- Wheeler, M., and G. N. Kiladis, 1999: Convectively coupled equatorial waves: Analysis of clouds and temperature in the wavenumber–frequency domain. *J. Atmos. Sci.*, **56**, 374–399.
- Yano, J.-I., M. W. Moncrieff, and W. W. Grabowski, 2002: Walker-type mean circulations and convectively coupled tropical waves as an interacting system. *J. Atmos. Sci.*, **59**, 1566–1577.
- Yasunaga, K., and Coauthors, 2006: Melting layer cloud observed during R/V *Mirai* Cruise MIR01-K05. *J. Atmos. Sci.*, **63**, 3020–3032.
- Zhang, C., 1993: Large-scale variability of atmospheric deep convection in relation to sea surface temperature in the tropics. *J. Climate*, **6**, 1898–1913.